SUPPLEMENTARY MATERIAL

Tumor-derived extracellular vesicles inhibit osteogenesis and exacerbate myeloma bone disease

Supplementary Methods and Materials

Isolation of cirEVs

Briefly, all participants fasted for 10 h before the samples were collected. Blood samples were collected from each individual using 21-gauge needles, and the samples were placed in BD Vacutainers containing EDTA. For all samples, the first 2 mL collected following venipuncture were discarded. Within 2 h of sample collection, platelet-free plasma (PFP) was obtained using double centrifugation at 2,500 $\times g$ for 30 min. The supernatants were then collected and PFP aliquots were stored at 4 °C for up to 2 weeks before they were used. The PFP was centrifuged at 16,000 $\times g$ for 15 min at 4 °C to obtain an EV pellet, and the centrifuge tube was then tipped to discard the supernatant, which left the pellet at the bottom undisturbed. Then, the EV pellet was resuspended in 100 μL of PBS using gentle vortexing for 20 s and immediately analyzed using flow cytometry (FCM) with a BD LSR II flow cytometer (BD Biosciences, San Jose, CA, USA) equipped with FACSDiva software.

MiRNA extraction, sequencing and analysis

We performed RNA-Seq and small RNA-Seq using HiSeq 2000. The raw sequences were processed to remove the vector sequences and filter the low quality bases, and

the clean reads with lengths from 15 to 30 nt were obtained. We used BWA to align the clean data to the human reference genome and BLAST to filter the other non-coding RNAs (i.e., rRNA, tRNA, snRNA, snoRNA) and mRNA degradation fragments from the aligned reads [1]. Finally, we used miRExpress to calculate the expression of the miRNAs in miRbase [2, 3]. We normalized the expression levels as the miRNA reads per million reads (RPM), which was calculated as 1,000,000× read counts/total clean reads. We investigated the miRNAs that were previously reported to be associated with bone regulation and cell proliferation. Then, the expression levels of those miRNAs were compared between the R-EVs and K562-EVs. Next, miRNA expression heat map graphs of these osteogenesis- and osteoclast-associated miRNAs were produced using MEV software with the log2 of RPM [4]. MiRNA target prediction was performed by integrating multiple prediction methods and databases according to methods described in our previous studies.

In vitro osteogenic differentiation of BM-MSCs

BM-MSCs were seeded in 6-well plates in medium containing 10 nM dexamethasone (Sigma), 50 μg/mL ascorbic acid and 5 mM β-glycerophosphate. The medium was supplemented with HMCL cell medium (20% v/v), conditioned HMCL medium (20% v/v) or RPMI-1640 medium and changed every 3 d during the assays to evaluate the effect of the HMCL medium on BM-MSC osteogenetic differentiation. To evaluate the effects of MM-EVs on osteogenesis in BM-MSCs, the medium was supplemented with or without MM-EVs at 50 ng/mL and changed every 3 d. The cells were

harvested to analyze osteogenic gene expression using real-time PCR every 3 d until day 6. The following primers were used: *β-actin*, sense 5'-GTCCACCGCAAATGCTTCTA-3' and anti-sense 5'-TGCTGTCACCTTCACCGTTC-3'; *ALP*, sense 5'-GCATAACATCAGGGACATTG-3' and anti-sense 5'-TGAAGTGGGAGTGCTTGTATC-3'; *RUNX2*, sense 5'-CTTGACCATAACCGTCTTCAC-3', anti-sense 5'-CTTCTGTCTGTGCCTTCTGG-3'; and *Collagen I,* sense 5'-CTTCACCTACAGCGTCACTG-3' and anti-sense 5'-GGATGGAGGGAGTTTACAGG-3'.

The level of secreted osteocalcin was detected using an ELISA (Abcam, Cambridge, UK) every 3 d until day 12, and ALP activity was examined using an ELISA (Boster, Wuhan, China) on days 3, 6 and 12. On days 14 and 21, the cells were stained for ALP (Baso Cell Science & Technology Co., Ltd., Zhuhai, China) and with Alizarin Red (Cyagen Biosciences Inc., Guangzhou, China) to quantify the number of CFU-Fs and CFU-OBs, respectively.

Cell apoptosis analyses

Apoptotic BM-MSCs were detected using FACS with a Bender MedSystems Human Annexin-V FITC kit according to the manufacturer's instructions. Briefly, BM-MSCs were seeded at P2 in 6-well plates at $3 \times 10^3/cm^2$ and cultured as described above. The cells were allowed to attach overnight (24 h). Then, the cells were cultured for another

2 weeks with or without MM-EVs, and the medium was replaced every 3 d. For the staining experiments, the cells were washed twice with $1\times$ PBS, resuspended and then incubated in 195 μL of $1\times$ binding buffer mixed with 5 μL Annexin V-FITC antibody solution for 10 min at room temperature. Finally, the cells were resuspended in the dark on ice in 190 μL of $1\times$ binding buffer that had been mixed with 10 μL of PI. The cells were then subjected to flow cytometry analysis.

Confocal microscopy

The EVs were stained using Annexin V-FITC (Beyotime Biotechnology, Suzhou, China), PKH-26 (Sigma-Aldrich, St. Louis, MO) and anti-CD138 (BD Biosciences, San Jose, CA, USA). To observe the uptake of MM-EVs into the BM-MSCs or MM cells, the MM-EVs were stained with PKH26 (1 μM), and the cells were then incubated with the PKH26-stained MM-EVs for 2, 4, 6, 12 or 24 h at 37 °C. The cells were then washed twice in PBS, counterstained with DAPI (Beyotime Technology, Suzhou, China) and visualized using a confocal microscope.

Western blot analysis

The membranes were blocked in blocking buffer containing 5% skimmed milk in TBST and 3% bovine serum albumin and then incubated overnight at 4 °C with the appropriate antibodies: anti-Alix, anti-TSG101, anti-CD63, anti-MFGE8, anti-CD9 and β-actin (Cell Signaling Technology, Beverly, MA, USA). Horseradish peroxidase-labeled secondary antibodies were added, and the proteins were visualized

using an enhanced chemiluminescence kit (BeyoECLPlus, Beyotime, Suzhou, China). The final results were analyzed using a Gel-Pro Analyzer (Media Cybernetics).

Animal studies

All experiments were performed in strict accordance with the recommendations described in the Guide for the Care and Use of Laboratory Animals of the National Institutes of Health. All surgeries were performed under sodium pentobarbital anesthesia, and all efforts were made to minimize suffering. BALB/c-nude mice were purchased from HuaFukang Bioscience Company (Beijing, China). Female mice (6–8 weeks old) were randomly assigned to the different treatment groups. The mice were acclimatized to the Specific Pathogen-Free (SPF) animal housing facility for a minimum period of 1 week before the start of the experiments. The animal housing facility was maintained under well-controlled conditions at a constant temperature (22 $\pm$ 2 °C) and humidity (55 $\pm$ 5%) and with a 12 h/12 h light/dark cycle. The animals were provided access to food and water *ad libitum*.

Briefly, RPMI8226 cells in log-phase growth were aspirated into a 50 μL Hamilton syringe (Alltech Associates) that was coupled to a 27-gauge needle. The needle was inserted through the cortex of the anterior tuberosity of the left tibia. Once the bone cortex was traversed, the needle was inserted 3 to 5 mm down the diaphysis of the tibia, and 30 μL of the cell suspension ($2\text{-}3\times10^{6}$ cells per inoculum) with/without MM-EVs was injected into the marrow space: serum-free RPMI-1640 medium (Control), $2\text{-}3\times10^{6}$ cells suspended in serum-free RPMI-1640 medium (MM),

2-3×10^6 cells mixed with 12.5 µg/µL of MM-EVs (MM+MM-EVs), or 12.5 µg/µL MM-EVs alone (MM-EVs). The sample size was statistically determined and blinding was used.

Ex vivo micro-computed tomography imaging and analysis

The tibiae collected for micro-CT imaging were surgically resected and fixed in formalin. Each bone was scanned at an isotropic voxel size of 15 µm using a ZKKS-MCT-Sharp micro-CT scanner (Kai Sheng Medical Technology Co., Ltd. Guangzhou, China). The exposure parameters were 60 kV and 40 W. The scan frames were set to 6. To analyze the cortical bone lesions, cross-sectional images of the entire metaphysis, including the cortices and extending 0.25 mm from the growth plate, were imported into the MedProject 4.1 System (3D graphics software, Guangzhou, China). This 3D graphics software was used to generate a 3D reconstruction of the metaphyses using a consistent threshold. The number of osteolytic lesions that completely penetrated the cortical bone in the virtual reconstruction was counted. A micro-CT parameter analysis was also performed on the trabecular bone to assess the overall volume and structural characteristics of the trabeculae. This analysis provided a ratio measurement of the bone volume to the total tissue volume within the cortical bone.

Bone histological and cytochemical analyses

Mice were deeply anesthetized with pentobarbital and euthanized by cervical

dislocation. The tibiae were fixed in 10% (v/v) buffered formalin for 24 h at 4 °C and then placed in 0.5 M EDTA/0.5% paraformaldehyde in PBS (pH 8.0) at 4 °C for 1-2 weeks for decalcification. The tibiae were then paraffin-embedded. Longitudinal sections (3 μm-thick) were prepared and stained with hematoxylin and eosin (H&E, Boster, Wuhan, China). In addition, tartrate-resistant acid phosphatase (TRAP, Beyotime, Suzhou, China) staining was used as a marker of osteoclast (OC) activity. In these assays, the number of TRAP[+] multinucleated OCs per bone surface was counted. Using Gomori's trichrome staining (Roche, Basel, Switzerland), osteocyte viability was evaluated out of a total of 500 lacunae per histological section. For the immunohistochemical analysis, sections (3 μm-thick) were deparaffinized in xylene, rehydrated in ethanol, and rinsed in PBS before being processed for antigen retrieval using a microwave. The tissues were peroxidase-quenched using 3% hydrogen peroxide for 10 min and then reacted with 1:200 diluted osteocalcin antibodies (Santa Cruz, CA, USA), 1:50 diluted CD138 antibodies (Santa Cruz, CA, USA), or mouse IgG control antibodies. The assay was completed using a DAB immunoperoxidase kit (Invitrogen Life Technologies, Carlsbad, CA, USA). The sections were lightly counterstained using hematoxylin (Invitrogen Life Technologies, Carlsbad, CA, USA). Finally, the slices were mounted in neutral gum prior to microscopic examination, and the cells containing brown granules in the cytoplasm or nucleolus were considered to be positive. All analyses were performed using an Olympus CX41 microscope.

CirEV counting and detection

Forward-scatter (FSC) and side-scatter (SSC) light were set on a logarithmic scale, and the fluorescence channels were set for logarithmic gain. Calibration beads were used to set the EV gate (using 1 μm beads) and to calculate the cirEV counts (using 3 μm beads). The EVs were further stained with calcein-AM. The cirEVs were defined as particles < 1.0 μm in diameter that exhibited calcein-AM-positive staining. After the particles were labeled with calcein-AM for 25-30 min in the dark, individual cirEV samples were diluted to a final volume of 300 μL. Then, calibration beads (3 μm diameter in 0.5 μL) were added immediately before the analysis. The gain settings were adjusted to place the 3 μm bead in the top right corner for scatter. Data acquisition was stopped when the number of events in the 3 μm bead gate reached 100,000. The counts for the cirEVs were calculated using a previously published equation [5].

Individual samples of isolated cirEVs (100 μL) were incubated with a mixture of antibodies against the surface markers and calcein-AM for 25-30 min in the dark. Additionally, fluorescence minus one controls were prepared for each marker to reveal the boundary between the positively and negatively labeled EVs [6]. After the cells were incubated, the volume was expanded to 300 μL. Before the flow cytometry analysis was performed, the mixture was vortexed for 20 s. Fluorescent cross-talk was controlled using compensation adjustments. The compensation settings were established by acquiring separate and combined unstained and single color-stained tubes. The absolute counts of the CD138^{+}cirEVs and CD138^{+}CD38^{+}cirEVs were

analyzed and calculated using FACSDiva software Version 6.1.2. FlowJo software version 7.6.2 (Palo Alto, CA, USA) was used to determine the absolute counts of the CD138$^-$CD19$^+$cirEVs and CD38$^+$CD45$^-$cirEVs.

Statistical analysis

Survival curves were plotted using the Kaplan-Meier method. The Wilcoxon rank test was used for comparisons of the cirEV counts between the *de novo* patients and healthy donors, between the newly diagnosed and relapsed patients, and between the *de novo* patients with normal and higher CRP levels. To analyze the differences in the cirEV counts across the *de novo* patients in different stages of the disease, the Wilcoxon rank test and Kruskal-Wallis test were used to compare stage 2 vs. 3 and 1 vs. 2 vs. 3 in a DS and ISS staging system, respectively. The Wilcoxon rank test and Kruskal-Wallis test were used to calculate the differences in the cirEV counts across the patients with bone lesions who were divided into two ($\leq$ 3 and > 3) and three (0, $\leq$ 3 and > 3) groups, respectively. The Kruskal-Wallis test was used to compare the cirEV counts between the *de novo* patients with different levels of β2-MG or different Ig types. Correlations between the cirEV counts and multiple serum factors or BMPC% were calculated using the Spearman's correlation test. ROC curves were used to determine the sensitivity, specificity, and positive and negative predictive values.

References

1. Li H, Durbin R. Fast and accurate long-read alignment with Burrows-Wheeler transform. Bioinformatics. 2010; 26: 589-595.

2. Wang WC, Lin FM, Chang WC, Lin KY, Huang HD, Lin NS. miRExpress: Analyzing high-throughput sequencing data for profiling microRNA expression. BMC Bioinformatics. 2009; 10: 1-13.

3. Kozomara A, Griffiths-Jones S. miRBase: annotating high confidence microRNAs using deep sequencing data. Nucleic Acids Res. 2014; 42: D68-D73.

4. Howe E, Holton K, Nair S, Schlauch D, Sinha R, Quackenbush J. MeV: MultiExperiment Viewer. In: Ochs M, Casagrande J, Davuluri R, Ed. Biomedical Informatics for Cancer Research. Boston, MA: Springer; 2010: 267-277.

5. Sun L, Wang HX, Zhu XJ, Wu PH, Chen WQ, Zou P, et al. Serum deprivation elevates the levels of microvesicles with different size distributions and selectively enriched proteins in human myeloma cells in vitro. Acta Pharmacol Sin. 2014; 35: 381-393.

6. Feher K, Kirsch J, Radbruch A, Chang HD, Kaiser T. Cell population identification using fluorescence-minus-one controls with a one-class classifying algorithm. Bioinformatics. 2014; 30: 3372-3378.

Supplementary Tables and Figures

Table S1. Characteristics of the *de novo* MM patients used to analyze the levels of PB CD138$^+$CD38$^+$cirEVs.

Table S2. Characteristics of *de novo* MM patients used to analyze the levels of PB CD138$^-$CD19$^+$cirEVs and CD38$^+$CD45$^-$cirEVs.

Figure S1. Characteristics of MM-EVs.

Figure S2. Inhibited osteogenesis differentiation without significantly affected proliferation and apoptosis in BM-MSCs by MM-EVs.

Figure S3. Infused MM-EVs into MM cells and stimulated proliferation in MM cells by MM-EVs.

Figure S4. Correlations between PB circulating CD138$^+$cirEV counts and clinical features in MM patients.

Figure S5. Association between the levels of PB CD138$^+$cirEVs and genetic lesions.

Figure S6. Correlation between the levels of CD138$^+$CD38$^+$cirEVs and clinical features in D-MM patients.

Figure S7. Correlations between PB CD138$^-$CD19$^+$cirEV counts and clinical features of D-MM patients.

Figure S8. Correlations between PB CD38$^+$CD45$^-$cirEV counts and clinical features in D-MM patients.

Figure S9. EV gating strategy.

Table S1. Characteristics of the *de novo* MM patients used to analyze the levels of PB CD138$^+$CD38$^+$cirEVs.

	Numbers or value
Patients (*n*)	40
Sex (*n*)	
Male	29
Female	11
Median age, years(range)	59(40-76)
Durie-Salmon stage(*n*)	
1	0
2	6
3	25
NA	9
Serum creatinine(*n*)	
<2mg/dL	23
≥2mg/dL	8
NA	9
International staging system(*n*)	
1	4
2	14
3	18
NA	4
Type of monoclonal Ig(*n*)	
IgG	20
IgA	8
IgD	1
LC	4
NA	7
Bone lesions (*n*)	
None	16
≤ 3	16
> 3	8
C-reactive protein (*n*)	
1	15
2	17
NA	8
β2-microglobulin, mg/L, *n* = 36, median(range)	4.45(1.7-20)
LDH, mM, *n* = 35, median(range)	158(90-429)
Serum calcium, mM, *n* = 40, median(range)	2.12(1.37-3.54)
Median albumin, mg/L, *n* = 38, median(range)	31.05(18.7-44.8)
Bone marrow plasma cell, %, *n* = 16, median (range),	24.75(4.5-91)

LC, light chain; NA, unavailable.

Table S2. Characteristics of *de novo* MM patients used to analyze the levels of PB CD138$^-$CD19$^+$cirEVs and CD38$^+$CD45$^-$cirEVs.

|	Numbers or value
Patients (*n*)	22
Sex (*n*)	
Male	15
Female	7
Median age, years(range)	57(40-76)
Durie-Salmon stage(*n*)	
1	0
2	6
3	16
Serum creatinine(*n*)	
<2mg/dL	15
≥2mg/dL	7
International staging system(*n*)	
1	2
2	10
3	7
NA	3
Type of monoclonal Ig(*n*)	
IgG	10
IgA	4
IgD	1
LC	3
NA	4
Bone lesions (*n*)	
None	2
≤ 3	14
> 3	6
C-reactive protein (*n*)	
1	6
2	10
NA	6
β2-microglobulin, mg/L, *n* = 19, median(range)	4.1(1.7-20)
LDH, mM, *n* = 20, median(range)	166(106-429)
Serum calcium, mM, *n* = 20, median(range)	2.2(1.37-3.54)
Albumin, mg/L, *n* = 20, median(range)	30.6(23.3-44.8)
Bone marrow plasma cell, %, *n* = 16, median(range)	24.75(4.5-91)

LC, light chain; NA, unavailable.
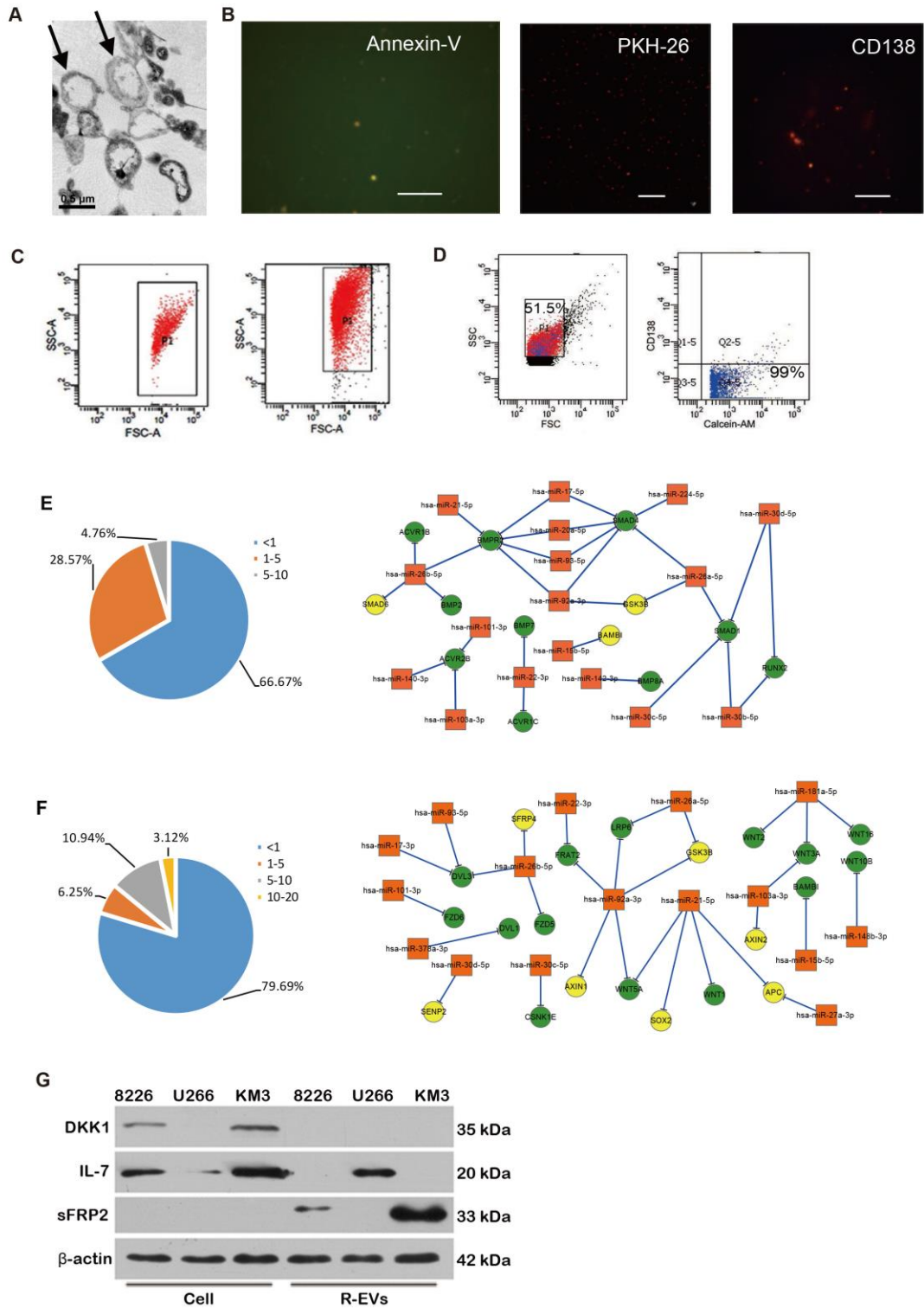
Figure S1. Characteristics of MM-EVs. (A) Transmission electron microscopy

revealing that the purified EVs (arrows) are 100-1000 nm vesicles that were shed

from U266 cells. *Arrow*s show EVs with spherical shapes. Scale bar, 500 nm (×

25600). **(B)** Confocal microscopy images of Annexin-V-stained, PKH-26-stained and anti-CD138-stained EVs. Scale bar, 20 μm. **(C)** The microbead gating (1 μm) used for the PS (left) and CD138 (right) expression analyses shown in Figure 1C. **(D)** Representative FACS analysis of peripheral CD138$^+$cirEVs obtained from healthy donors (n = 29). Left: microbead gating (1 μm); right: CD138$^+$Calcein-AM$^+$cirEVs gating. **(E-F)** Distributions of the expression profiles of genes in the BMP (E) and WNT (F) signaling pathways and their regulatory networks to correspond to osteogenesis-associated miRNAs. The scales in the pie graph indicate the gene expression profile of RPKM. The miRNA targets were experimentally validated targets that were collected from multiple databases. In the networks, red rectangles indicate miRNAs, circles indicate genes belonging to the pathway, and yellow circles indicate inhibitors of the pathway. **(G)** Western blot analysis the level of DKK1, IL-7 and sFRP2 in MM-EVs and their parental cells.
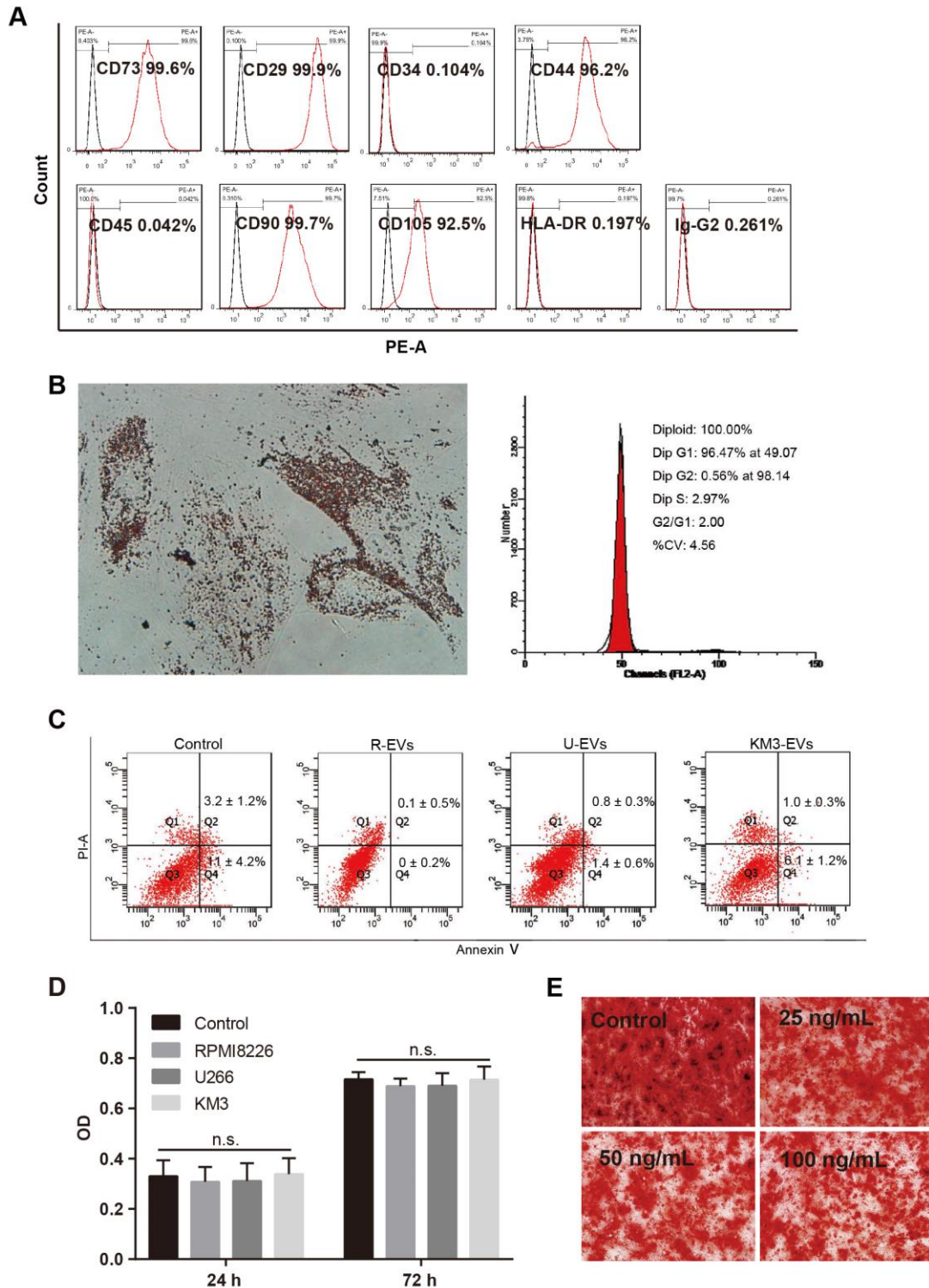
Figure S2. Inhibited osteogenesis differentiation without significantly affected proliferation and apoptosis in BM-MSCs by MM-EVs. **(A-B)** Validation of the results obtained using isolated BM-MSCs in flow cytometry analyses of surface

markers (A) and analyses of adipogenic differentiation (left) and the cell cycle(right) in BM-MSCs (B). **(C-D)** The effect of MM-EVs applied at 100 ng/mL on apoptosis (C) and proliferation (D) in BM-MSCs. **(E)** Alizarin Red staining of the dose-dependent assay of R-EVs (25, 50 and 100 ng/mL) on inhibiting osteogenic differentiation of BM-MSCs. All data are shown as the mean ± SD of more than three experiments. n.s. Signifies $P > 0.05$

Figure S3. Infused MM-EVs into MM cells and stimulated proliferation in hematological malignant cells. (A) Confocal microscopy revealing the fusion of PKH26-staining (red) MM-EVs that were secreted by RPMI 8226 cells with their parental RPMI 8226 cells, which were counterstained with DAPI (blue). RPMI 8226

1   cells were cultured with R-EVs, and PKH26-stained R-EVs were observed around the

2   DAPI-staining nuclei of the MM cells after 6, 12 and 24 h. Arrows indicate MM-EVs

3   that infused into the MM cells and were located around the nuclei. **(B)**

4   MM-EV-induced cell activity in HMCLs (RPMI 8226 and U266). HMCLs (5×10^4)

5   were cultured in the wells of 96-well plates with or without (control) the indicated

6   MM-EVs (50 ng/mL). The growth rates were determined using MTT tests (1 and 2). 3:

7   Proliferation in HMCLs that were treated with the indicated MM-EVs that were

8   applied at various concentrations from 5 to 100 ng/mL. **(C)** ELISA and QPCR

9   analyses of the expression of IL-6.

10

11
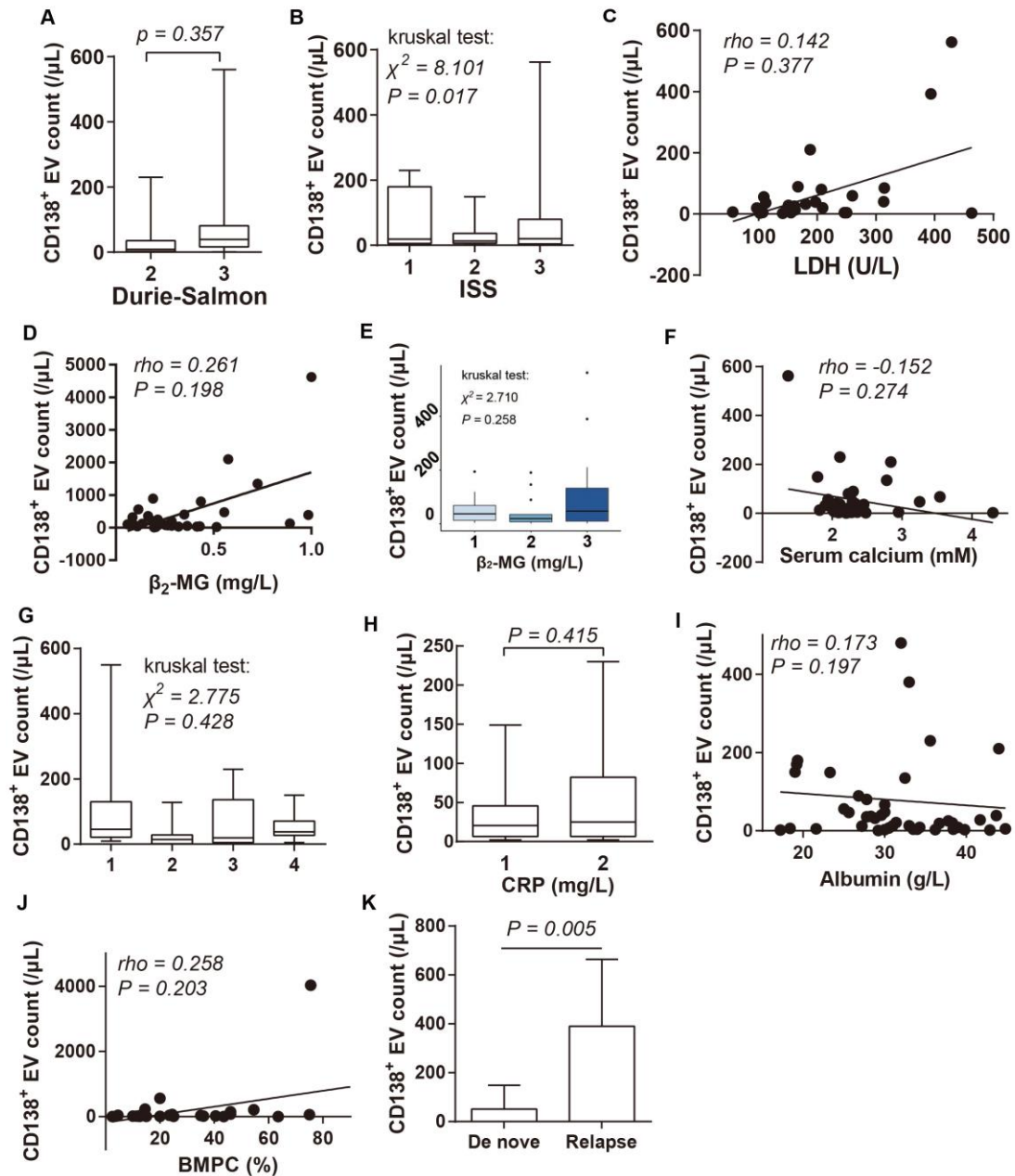
Figure S4. Correlations between PB circulating CD138$^+$cirEV counts and clinical features in MM patients. **(A-B)** The difference in the CD138$^+$cirEV counts between the D-MM patients in stage 1-2 (n = 14) and stage 3 (n = 38) (Durie-Salmon) (A), and among patients with stage 1-3 disease according to the ISS grading system (n = 58) (B). **(C)** Correlations between the levels of PB CD138$^+$cirEVs and the levels of LDH (n = 48). **(D-E)** Correlation between the CD138$^+$cirEV counts and β2-microglobulin

1   (β2-MG) level in the D-MM patients (n = 57) (D), and the differences in the levels of

2   PB CD138$^+$cirEVs among patients with different levels of β2-MG (1: < 3.5 mg/L; 2:

3   3.5-5.5 mg/L; 3: ≥ 5.5 mg/L; n = 57) (E). **(F)** Correlations between the levels of PB

4   CD138$^+$cirEVs and the levels of serum calcium in newly diagnosed MM patients (n =

5   56). **(G-H)** Differences in the levels of PB CD138$^+$cirEVs among patients with the

6   indicated type of monoprotein (1-4 indicates IgG, IgA, IgD and light chain alone, the

7   groups of which contained n = 27, 16, 3 and 8 patients, respectively) (G) and between

8   *de novo* MM patients with CRP <3.45 (1, n = 27) and CRP ≥ 3.45 (2, n =22) mg/L (H).

9   **(I-J)** Correlations between the levels of PB CD138$^+$cirEVs and the levels of serum

10   albumin (g/L) (n = 59) (I) and BMPC% (n = 26) (J). **(K)** Comparative analysis of the

11   CD138$^+$cirEV counts between the D-MM patients (n = 55) and relapsed patients (n =

12   5). ISS, International Staging System; β2-MG, β2-Microglobulin; LDH, lactate

13   dehydrogenase; CRP, C-reactive protein; BMPC, bone marrow malignant plasma

14   cells.

15

16
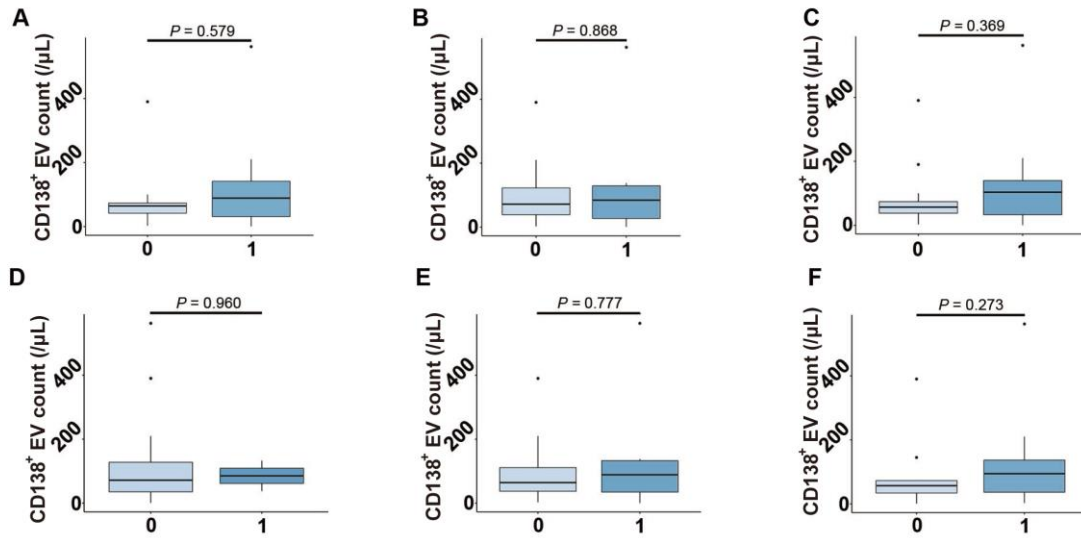
Figure S5. Association between the levels of PB CD138$^+$cirEVs and genetic lesions. Genetic lesions were detected using FISH, including del(13q14.3), amp(1q21), t(4;14) and an adverse *IGH* translocation in *de novo* MM patients. Difference in the levels of PB CD138$^+$EVs between patients with (n = 15) and without (n = 10) the detected lesions **(A)**, with less than or equal to one lesion (n = 15) and with more than one lesion (n = 10) **(B)**, with (n = 12) and without (n = 13) amp(1q21) **(C)**, with (n = 12) and without (n = 13) t(4;14) **(D)**, with (n = 9) and without (n = 16) del(13q14.3) **(E)**, and with (n = 14) and without (n = 11) an adverse *IGH* translocation**(F)**.
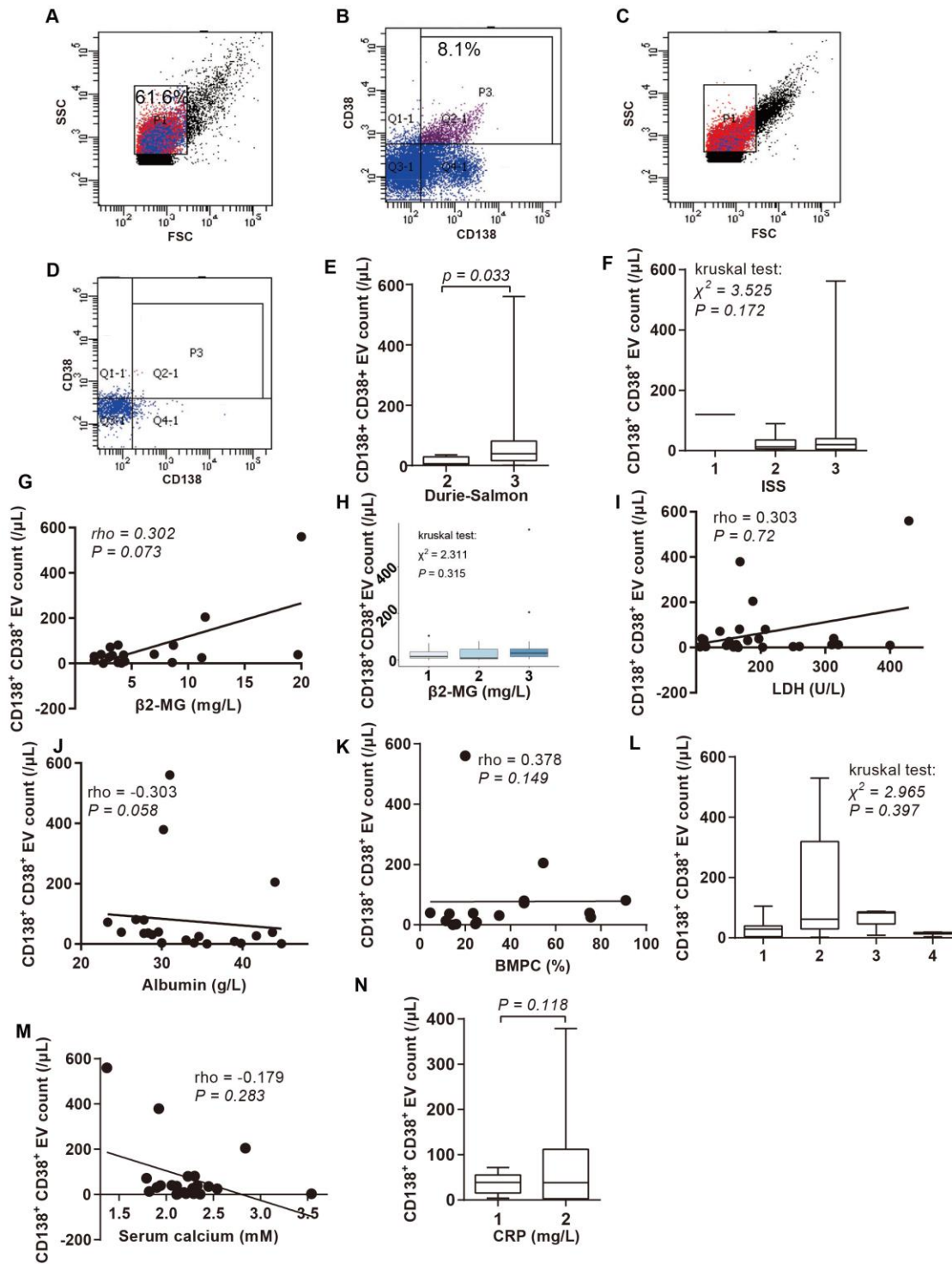
Figure S6. Correlation between the levels of CD138⁺CD38⁺cirEVs and clinical features in D-MM patients. **(A-D)** Representative FACS analysis to determine the levels of PB CD138$^+$CD38$^+$ cirEVs in newly diagnosed MM patients (A and B, n = 40)

1 and healthy donors (C and D, n = 29). The characteristics of these *de novo* patients

2 and healthy controls are shown in supplementary Table S2. **(E-F)** Comparative

3 analysis of the CD138$^+$CD38$^+$ cirEV counts between the D-MM patients in stage 1-2

4 (n = 6) and stage 3 (n = 25) (Durie-Salmon) (E)**.** The differences in the levels of PB

5 CD138$^+$CD38$^+$ cirEVs among patients with stage 1-3 disease according to the ISS

6 grading system (n = 40) (F). **(G-H)** Correlation between the CD138$^+$CD38$^+$cirEV

7 counts and β2-MG level in the D-MM patients (n = 40) (G), and the difference in the

8 CD138$^+$CD38$^+$ cirEV counts of D-MM patients with different levels of β2-MG (1:

9 <3.5 mg/L; 2: 3.5-5.5 mg/L; 3: ≥ 5.5 mg/L) (n = 36) (H). **(I-K)** Correlations between

10 the levels of PB CD138$^+$CD38$^+$cirEVs and the levels of LDH (I) (n = 35), serum

11 albumin (g/L, n = 38) (J) and BMPC% (n = 16) (k). **(L)** Differences in the levels of

12 PB CD138$^+$CD38$^+$cirEVs among patients with the indicated type of monoprotein (1-4

13 indicates IgG, IgA, IgD and light chain alone, which contained n = 20, 8, 1, 4, and 7

14 patients, respectively). **(M)** Correlations between the levels of PB

15 CD138$^+$CD38$^+$cirEVs and the levels of serum calcium (n = 40). **(N)** Differences in the

16 levels of PB CD138$^+$CD38$^+$cirEVs between patients with CRP <3.45 (1, n = 15) and
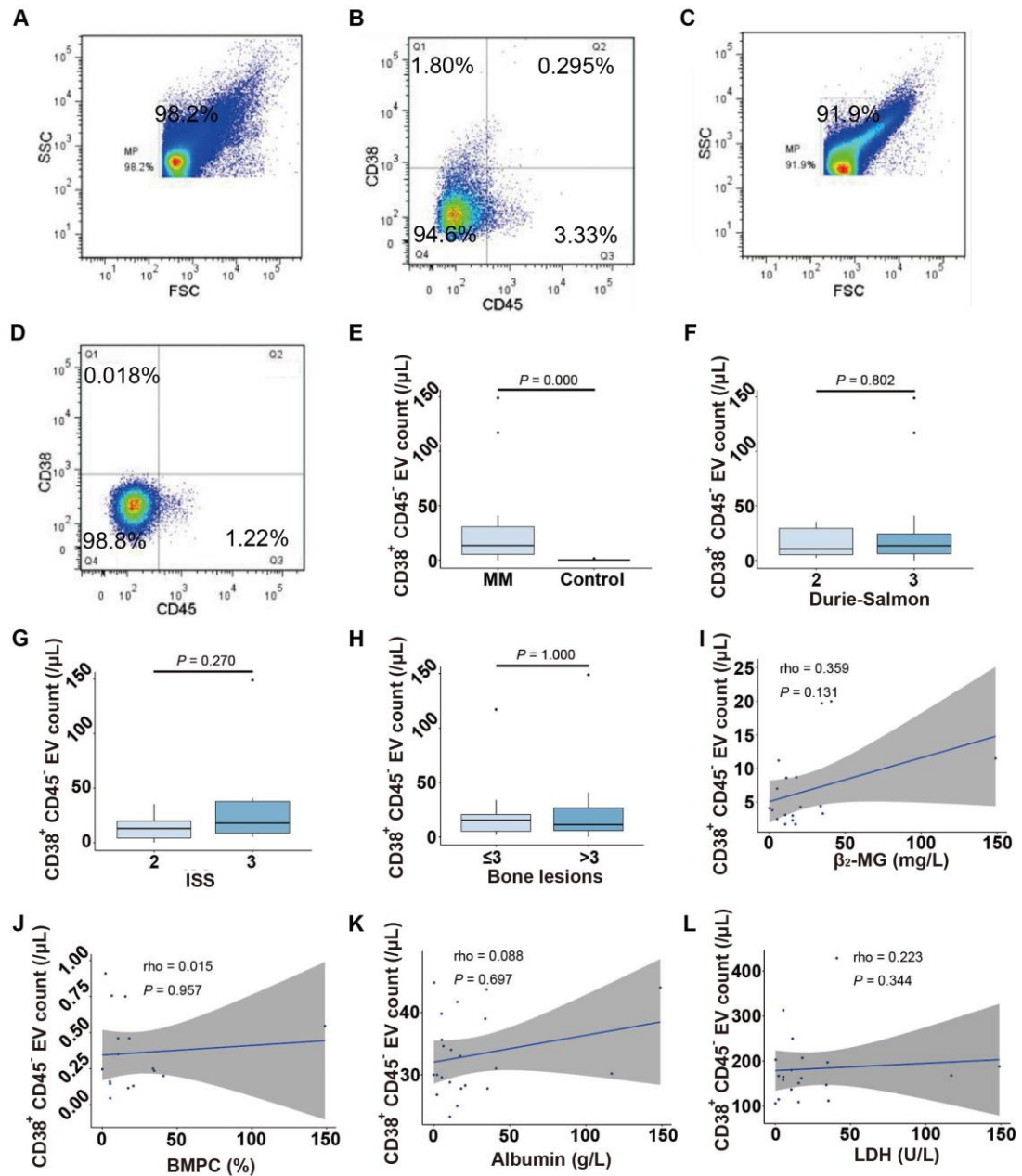
17 CRP ≥ 3.45 (2, n = 17) mg/L.

18

19
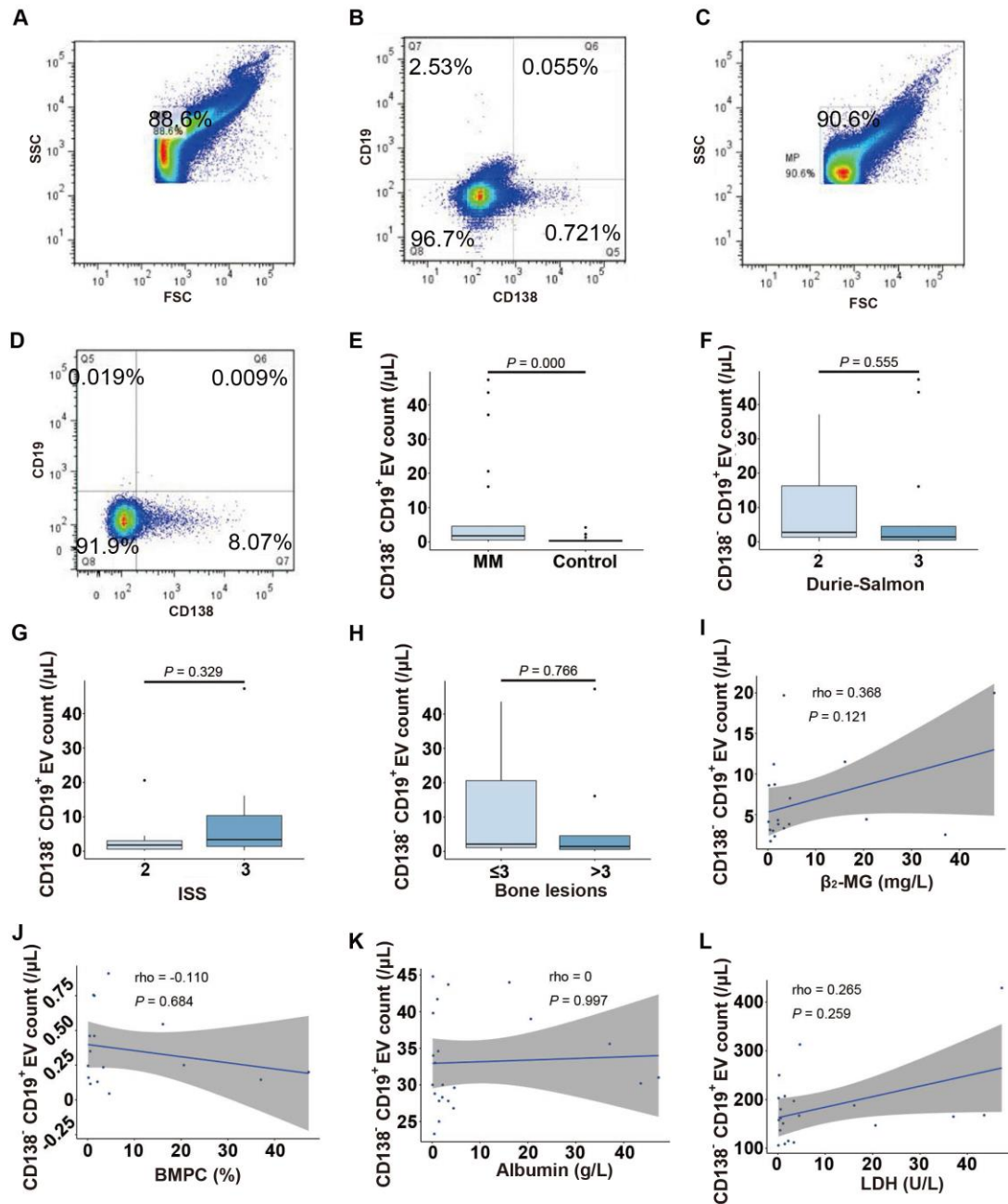
Figure S7. Correlations between PB CD138⁻CD19⁺cirEV counts and clinical features of newly diagnosed MM patients. **(A-D)** Representative FACS analysis of the levels of PB CD138⁻CD19⁺cirEVs in newly diagnosed MM patients (A and B, n = 22) and healthy donors (C and D, n = 29). **(E-H)** Differences in the levels of PB CD138⁻CD19⁺cirEVs between newly diagnosed MM patients and healthy donors (E),

1 between patients with stage 2 (n = 6) and 3 (n = 16) disease according to the

2 Durie-Salmon grading system (F), between patients with stage 2 (n = 10) and 3 (n = 7)

3 disease according to the ISS grading system (G), and between patients with ≤ 3 (1, n =

4 16) and > 3 (2, n = 6) bone lesions (H). **(I-L)** Correlations between the levels of PB

5 CD138$^-$CD19$^+$cirEVs with the levels of β2-MG (mg/L, n = 19) (I), BMPC% (n = 16)

6 (J)**,** serum albumin (g/L, n = 20) (K) and LDH (U/L, n = 20) (L).

7

8

Figure S8. Correlations between PB CD38$^+$CD45$^-$cirEV counts and clinical features in newly diagnosed MM patients. **(A-D)** Representative FACS analysis of the levels of PB CD38$^+$CD45$^-$cirEVs in newly diagnosed MM patients (A and B, n = 22) and healthy donors (C and D, n = 29). **(E-H)** Differences in the levels of PB CD38$^+$CD45$^-$cirEVs between newly diagnosed MM patients and healthy donors (E), between patients with stage 2 (n = 6) and 3 (n = 16) disease according to the

Durie-Salmon grading system (F), between patients with stage 2 (n = 10) and 3 (n = 7)

disease according to the ISS grading system (G), and between patients with ≤ 3 (1, n =

16) and > 3 (2, n = 6) bone lesions (H). **(I)** Correlations between the levels of PB

$CD38^+CD45^-$cirEVs and the levels of β2-MG (mg/L, n = 19), **(J)** BMPC% (n = 16),

serum albumin (g/L, n = 20) **(K)** and LDH (U/L, n = 20) **(L)**.
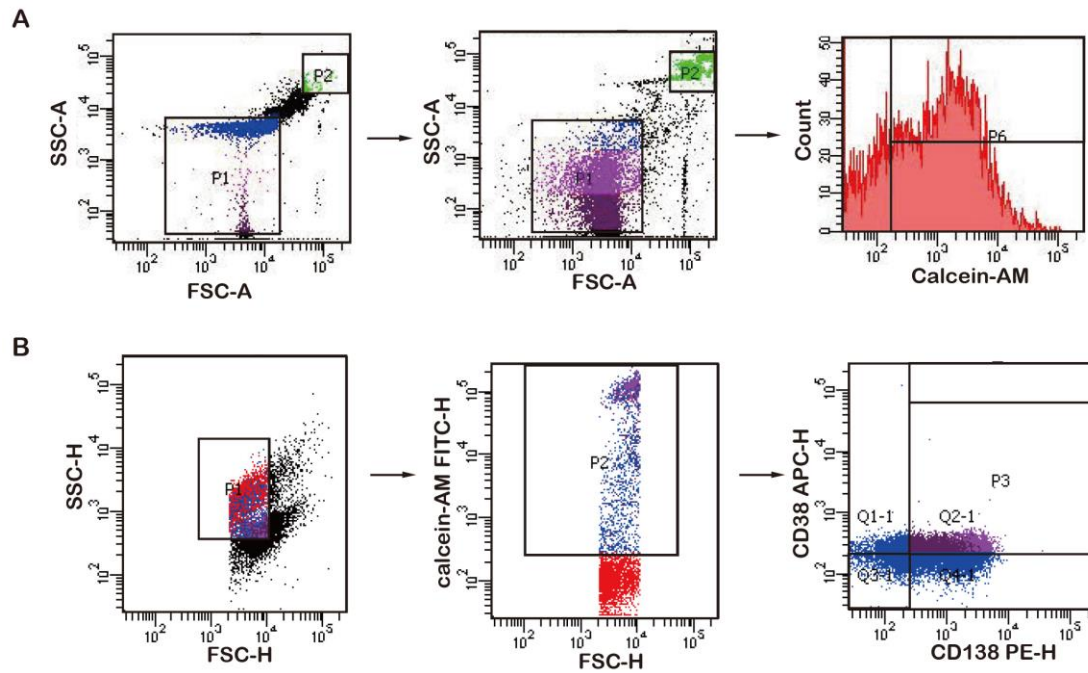
Figure S9. EV gating strategy. (A) Calculation of EV counts. The first plot gated for two standard microbeads (1 μm mean particle size and 3 μm particle size), and EVs were defined as particles smaller than 1 μm (P1 proportion). The second plot gated for the flow cytometry plots of EVs, and the microbeads (3 μm) (P2 proportion) were used as an internal standard. Counting end was set as 100,000 events in the P2 proportion. The third plot represented the integrity of EVs. **(B)** Detection of the surface markers of EVs. EVs were smaller than 1 μm (P1 proportion, first plot) and positive for calcein-AM (P2 proportion, second plot). The third plot indicated the expression of CD38 and CD138 in MM-EVs (P3 proportion).